Spin crossover in the CsFeII[Cr-III(CN)(6)] Prussian blue analog: Phonons and thermodynamics from hybrid functionals

Spin crossover in the $CsFe^{II}[Cr^{III}(CN)_6]$ Prussian blue analog: Phonons and thermodynamics from hybrid functionals

Derek S. Middlemiss,[1,2] Damiano Portinari,[1] Clare P. Grey,[2,3] Carole A. Morrison,[4] and Chick C. Wilson[1,*]

[1]*Department of Chemistry and WestCHEM Research School, University of Glasgow, University Avenue, Glasgow G12 8QQ, United Kingdom*

[2]*Department of Chemistry, State University of New York at Stony Brook, Stony Brook, New York 11794-3400, USA*

[3]*Department of Chemistry, University of Cambridge, Lensfield Road, Cambridge CB2 1EW, United Kingdom*

[4]*School of Chemistry and EaStCHEM, University of Edinburgh, Kings Buildings, West Mains Road, Edinburgh EH9 3JJ, United Kingdom*

(Received 16 September 2009; revised manuscript received 27 March 2010; published 12 May 2010)

Solid-state lattice-dynamics calculations within the hybrid density-functional approach are applied to the study of the thermally induced Fe^{2+} low spin(LS;$S=0$)$\leftrightarrow$high spin(HS;$S=2$) crossover (SCO) in the extended network of the $CsFe[Cr(CN)_6]$ Prussian blue analog. The variations in the thermodynamic parameters defining the SCO transition with the Fock exchange content (F_0) of the functional are obtained and discussed, where, in keeping with the findings of previous studies of isolated complexes, it is found that an admixture $F_0 \approx 14\%$ provides reliable values. The transition is shown to be dominated by the entropy difference, ΔS, associated with the softening of low-frequency vibrational (vib) modes in the HS state, as has been suggested previously for a wide range of SCO materials, more than half of ΔS_{vib} deriving from modes with wave numbers of 250 cm^{-1} or less. Analysis of the influence of the spectroscopic selection rules upon the apparent SCO thermodynamics reveals that determinations based solely upon infrared or Raman frequencies, or upon their combination, lead to significant errors. The effect upon the SCO transition of the electronic entropy associated with the degenerate Fe^{2+} HS ($e_g^2 t_{2g}^4$) configurations is also detailed, evidence for the existence of an associated dynamic Jahn-Teller distortion being presented. Optimized structures, bulk moduli, Γ-point vibrational frequencies, and crystal-field energy models are discussed for all relevant spin states.

DOI: 10.1103/PhysRevB.81.184410 PACS number(s): 75.30.Wx, 71.15.Nc, 71.20.Ps, 71.70.Ch

I. INTRODUCTION

Spin crossover (SCO) is a relatively rare class of spin state transition occurring within octahedrally coordinated transition-metal (TM) ions bearing d^4-d^7 electronic configurations. A variety of external perturbations have been shown to induce the effect, including variations in temperature and pressure, illumination, and exposure to magnetic fields.[1–7] SCO may be regarded as one example in a more general field of molecular electronic bistabilities, collectively of interest for their potential applications as fundamental elements in novel information processing and display technologies.[4] Such bistabilities are of technological use only insofar as they are associated with a readily observable response of the material, such as a change in volume, magnetization, electrical conductivity, or optical absorption. A careful choice of ligand, and ancillary metal species can couple the bistability to other properties of interest, including, for example, the appearance of magnetic, charge, or orbital ordering in one, or both of the metastable states. Specifying further to thermal SCO, it is clear that this occurs only in materials wherein the high-spin (HS) and low-spin (LS) states of the active TM are sufficiently close in energy, their separation being notionally within the range of the thermal energy. In turn, this requires near equality in the crystal-field splitting and spin-pairing energies. The scarcity of compounds displaying the effect comes directly from the restrictive nature of this criterion. Most examples to date involve octahedral (or near octahedral) $Fe^{II}N_6$ coordination, suggestive of a favorable disposition of the crystal-field parameters and intra-atomic interactions within this configuration.[8]

The recent reviews of Gütlich and Goodwin;[8] Ksenofontov *et al.*;[9] and Sato *et al.*[10] summarize the broad range of experimental techniques applied to SCO materials. Of particular interest here are those studies focusing upon the thermodynamics of the effect. Calorimetry is an obvious first choice and has been pursued for a range of materials.[11,12] However, the insights obtained are limited by difficulties in partitioning the derived quantities into contributions due to electronic, vibrational, and configurational degrees of freedom. Vibrational spectroscopy offers a complementary approach, namely, the determination of thermodynamical parameters directly from the mode frequencies, but this is often hampered by problems associated with incomplete spectra and unknown mode degeneracies. Nevertheless, useful insights have been obtained for a range of materials.[13–15] Atom-specific vibrational frequencies for a more limited set of compounds have also previously been obtained from nuclear inelastic scattering experiments.[16,17]

Examining theoretical approaches, high-level wave-function-based treatments of electron correlation are, in principle, possible for isolated complexes, but their computational intensiveness often renders geometry optimizations and normal-mode determinations impractical, limiting applications to SCO complexes. Hybrid density-functional theory (DFT) offers a reasonable compromise, the main limitation here arising in relation to the reliable prediction of the HS-LS splitting energy, and the typically strong dependence of this quantity upon the Fock exchange content [denoted F_0 (%) hereafter] of the functional. Investigations across a range of Fe^{II} complexes and functionals broadly concur that

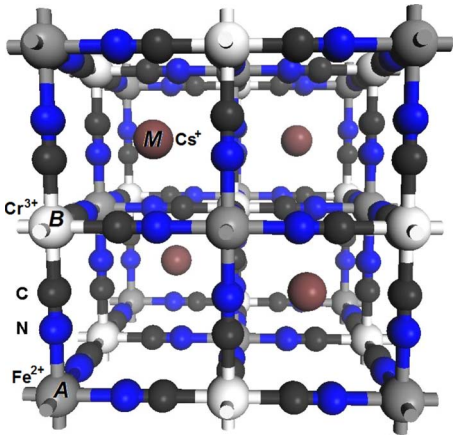

FIG. 1. (Color online) The $F\bar{4}3m$ symmetry conventional cell of $CsFe^{II}[Cr^{III}(CN)_6]$.

weights of Fock exchange in the low range $F_0=0-25$ % offer improved accuracies for specific materials.[18–22] More specifically, Daku *et al.*[21] recommended a value $F_0=10\%$ on the basis of the LS→HS transition in the $[Fe(bpy)_3]^{2+}$ (bpy=bipyridine) complex; Harvey,[22] $F_0=15\%$ on the basis of a general review of hybrid functionals for spin state energetics; and Reiher,[18] the same value on the basis of the LS→HS transition in the $Fe(phen)_2(NCS)_2$ (phen=phenanthroline) SCO complex. The recent review of Paulsen and Trautwein[23] provides a comprehensive overview of the application of DFT to SCO materials.

The current study addresses thermal SCO in the Prussian blue analog $Cs^IFe^{II}[Cr^{III}(CN)_6]$ (Fig. 1), the first such effect reported in this class of materials.[6,7] Here, increase in temperature leads to an Fe^{II} $LS(e_g^0t_{2g}^6:S=0)\rightarrow HS(e_g^2t_{2g}^4:S=2)$ transition at approximately 238 K, accompanied by an isosymmetric (space group $F\bar{4}3m$) lattice expansion of 0.38 Å.[6] The reverse transition (HS→LS) occurs at 211 K with decreasing temperature, consistent with a broad hysteresis approximately 30 K in width, and it is estimated that approximately 11% of the Fe^{II} sites remain in the HS configuration below the critical temperature.[6] The transition temperature was found to increase rapidly with pressure at the rate of 60 K $kbar^{-1}$ without appreciable change in the shape of the hysteresis loop.[7] Interestingly, it has also been shown that x-ray illumination can induce HS→LS conversion, fits of a nucleation model yielding a reaction rate that decreases with increasing temperature.[24] Combined diffraction, magnetic susceptometry, and infrared (IR) spectrometry measurements suffice to rule out the involvement of either internal TM redox or ligand isomerization processes in the SCO effect.[6,7] The magnetic measurements also indicate the onset of spin ordering in the LS state at approximately 9 K while mean-field theory fits to the $\chi_M T$ vs T curves on both sides of the SCO transition reveal ferromagnetic (FM) J_{CrCr} and $J_{Fe^{HS}Cr}$ exchange couplings with magnitudes 1.1 cm^{-1} and 1.9 cm^{-1}, respectively.[6]

The $CsFe^{II}[Cr^{III}(CN)_6]$ system has also been the subject of a previous theoretical study by Le Guennic *et al.*[25] High-level CASPT2 calculations were performed for $[Fe(NC)_6]^{4-}$ clusters embedded in point-charge arrays, focusing upon the variation in the HS-LS splitting energy as a function of the various charge models applied. Interestingly, it emerged that the inclusion of the charge reorganization across the LS→HS transition was necessary in order to achieve even qualitative agreement with experiment. However, the splitting of 150 kJ/mol provided by this study seems large in comparison with the predictions for other SCO materials.[18,26] Recently, Wojdeł *et al.*[27] have also performed periodic calculations for this system using the generalized gradient approximation plus U (GGA+U) method and the Heyd-Scuseria-Ernzerhof (HSE06) ($F_0=25\%$) screened hybrid functional. This study concluded that the Fe^{II} LS state is most stable in the experimental low-temperature structure and the HS state in the high temperature form. Geometry optimizations in both spin states using the GGA+U method reproduce the experimental magnitude of the lattice expansion across the LS→HS transition, the splitting energy as a function of cell volume also being investigated. Interestingly, the hybrid calculations also suggest that the HS state should be metallic, the Fermi energy falling within a narrow Fe(3d) band.[27]

The present study addresses the SCO effect in $CsFe[Cr(CN)_6]$ within a periodic DFT approach. Hybrid Hamiltonians with a wide range of F_0 values are considered so as to further characterize the accuracy of such functionals in describing solid-state SCO effects. Vibrational frequencies obtained within a harmonic lattice-dynamics approach are combined with static energetics to compute transition temperatures and associated thermodynamic parameters. The latter results are of particular interest given the paucity of solid-state vibrational calculations for SCO compounds. The present approach is partly motivated by the implication of previous studies that periodic simulations naturally incorporating intermolecular interactions may more accurately describe the transition thermodynamics in related materials.[23,28] It is also of interest to identify those modes not observable by IR or Raman spectroscopy and to determine whether their omission significantly alters the derived thermodynamic parameters. This will provide insight into the accuracy of these experimental techniques in determining the thermodynamics of not only the present compound but of the solid phases of SCO materials in general.

The paper is structured as follows: the thermodynamical model of the SCO transition is detailed first, followed by a description of the computational method. Preliminary analyses of the spin excitation energies in terms of a crystal-field Hamiltonian are then presented with the aim of determining the relevant spin states for the subsequent DFT calculations. Results relating to equilibrium geometries and static LS→intermediate spin (IS) and LS→HS excitation energies follow, while the final section details the vibrational and thermodynamic properties obtained from the lattice-dynamics calculations, and also presents the main findings in regard to the performance of the various hybrid functionals in describing the SCO transition. The Supplementary Material[61] provides results and analyses relating to the electronic structures of the various spin states and the magnetic coupling in the HS phase along with a representative set of normal-mode eigenvectors for the LS and HS phases.

II. THERMODYNAMIC MODEL OF THE SPIN CROSSOVER TRANSITION

Thermal SCO occurs when the enthalpy difference $\Delta H(T)$ separating ground (LS) and excited (HS) states is overcome by the entropic contribution $T\Delta S(T)$, such that $\Delta H(T_{1/2}) = T_{1/2}\Delta S(T_{1/2})$, where $T_{1/2}$ denotes the crossover temperature at which the fraction of HS SCO-active sites, $\gamma(T)$, equals one half. The entropy difference $\Delta S(T)$ driving the transition arises out of the increase in the spin and effective vibrational degeneracies in the HS state. The former temperature-independent contribution, $\Delta S_{\text{spin}} = R\ln(\frac{2S_{\text{HS}}+1}{2S_{\text{LS}}+1})$, is usually smaller than the latter, $\Delta S_{\text{vib}}(T)$.[13,14,29] Typical values for octahedral Fe^{II} SCO complexes are 13.38 and approximately 22–66 J/K(mol Fe), respectively, the latter obtained in the vicinity of $T_{1/2}$.[13] The increased orbital degeneracy (g) of the HS state also leads to a contribution $\Delta S_{\text{orb}} = R\ln(\frac{g_{\text{HS}}}{g_{\text{LS}}})$, amounting to 9.13 J/K(mol Fe) for Fe^{II},[30] though it has been argued that Jahn-Teller (JT) distortion will generally lift this degeneracy.[11,14] Nevertheless, the present study considers the effects of both including and excluding ΔS_{orb}.

Numerous models of cooperative SCO transitions have been proposed, including the "Mainz" elastic model of Spiering *et al.*,[31] the cooperative domain model of Sorai and Seki,[29] and the Ising-type model of Wajnflasz.[32] As a working theory, the present study adopts the conceptually straightforward modified regular solution model first proposed for SCO materials by Slichter and Drickamer.[33] Here it is supposed that the Gibbs energy of the lattice, $G=U+pV-TS$, varies in some explicit fashion with γ, the equilibrium fraction satisfying the condition

$$\left.\frac{\partial G}{\partial \gamma}\right|_T = 0, \tag{1}$$

where, as in what follows, the explicit pressure dependence has been neglected. More specifically, it is assumed that the molar Gibbs energy includes a contribution varying linearly with γ from a value $G_{\text{LS}}(T)$ for the pure LS phase $(\gamma=0)$, to $G_{\text{HS}}(T)$ for the pure HS phase $(\gamma=1)$, such that

$$G = (1-\gamma)G_{\text{LS}}(T) + \gamma G_{\text{HS}}(T) + \Phi(T)\gamma(1-\gamma) + RT[\gamma\ln\gamma + (1-\gamma)\ln(1-\gamma)]. \tag{2}$$

The term involving Φ introduces interactions between HS and LS sites: small or zero values corresponding to only weakly or noncooperative transitions; and large values, to strong cooperativity with the potential for discontinuity and hysteresis in the $\gamma(T)$ curve. The experimental findings outlined above suggest that SCO in $CsFe[Cr(CN)_6]$ is of the discontinuous and strongly hysteretic type.[6,7] The final term represents the mixing entropy of a random solution of composition $HS_\gamma LS_{1-\gamma}$. Assuming pairwise-additive nearest-neighbor (nn) interactions, the interaction constant may be expressed

$$\Phi = N_{\text{A}}\frac{z}{2}(2\varepsilon_{\text{HS,LS}} - \varepsilon_{\text{HS,HS}} - \varepsilon_{\text{LS,LS}}), \tag{3}$$

where N_{A} is Avogadro's constant; z, the effective coordination number; $\varepsilon_{\text{HS,LS}}$, the interaction energy of a nn HS$\cdots$LS pair; and similar for $\varepsilon_{\text{LS,LS}}$ and $\varepsilon_{\text{HS,HS}}$. Positive Φ values correspond to repulsive HS$\cdots$LS interactions within this convention. Combining Eqs. (1) and (2) yields

$$\Delta G(T) + \Phi(T)[1-2\gamma(T)] + RT\ln[K(T)] = 0, \tag{4}$$

where $\Delta G(T) = G_{\text{HS}}(T) - G_{\text{LS}}(T)$ and $K(T) = \gamma(T)/[1-\gamma(T)]$ is the equilibrium constant. Thus, it is clear that neither the interaction nor the entropy term contribute at $\gamma=\frac{1}{2}$ within this model, so that $\Delta G(T)=0$ at SCO. However, Φ retains a key role in determining the nature of the transition, as is evident from the following analog of the van't Hoff relationship derived in the presence of the interaction term

$$\frac{d\ln K(T)}{d(T^{-1})} = -\frac{1}{R}\frac{\Delta H + \left[\frac{1-K(T)}{1+K(T)}\right]\left[\Phi(T) - T\frac{d\Phi(T)}{dT}\right]}{1 - \frac{2\Phi(T)}{RT}\left\{\frac{K(T)}{[1+K(T)]^2}\right\}}, \tag{5}$$

where ΔH is the enthalpy difference. In the SCO region at $K=1$, it emerges that positive values of $\Phi(T_{1/2})$ approaching a critical value $\Phi_{\text{C}}=2RT_{1/2}$ lead to a singularity in $d\ln K(T)/d(T^{-1})$ corresponding to the strongly cooperative and discontinuous SCO transition discussed above.

The free energies of the LS and HS lattices are obtained from Γ-point lattice-dynamics calculations in the present work. The effects of phonon dispersion are neglected to maintain computational tractability, although a study addressing this topic in a more limited set of Hamiltonians is planned. Thus, while the present approach is restricted, support for it emerges from the fact that the majority of the experimental spectroscopic studies discussed above accessed only the zone-center frequencies, some proceeding to compute ΔS_{vib} on this basis.[13–15] However, as mentioned previously, analyses of this type often encounter difficulties in relation to undetermined degeneracies and silent or weakly absorbing modes. First-principles lattice-dynamics calculations can mitigate such problems, offering a complete determination of the vibrational spectrum of the solid.

A crystal cell containing N atoms possesses $3N$ normal modes of vibration, three of which are of acoustic type with frequencies $\omega_{1,2,3}=0$ at the Γ-point. For the remaining $3N-3$ optical modes with finite angular frequencies $\omega_{i=4,\ldots,3N}$, the harmonic molar zero-point energy (ZPE), enthalpy and entropy contributions are obtained as

$$E_{\text{ZPE}}^{\Gamma,i} = \tfrac{1}{2}N_{\text{A}}\hbar\omega_i,$$

$$H_{\text{vib}}^{\Gamma,i}(T) = N_{\text{A}}\hbar\omega_i\frac{e^{-\beta\hbar\omega_i}}{1-e^{-\beta\hbar\omega_i}},$$

$$S_{\text{vib}}^{\Gamma,i}(T) = -N_{\text{A}}k_{\text{B}}\ln(1-e^{-\beta\hbar\omega_i}) + \frac{N_{\text{A}}\hbar\omega_i}{T}\frac{e^{-\beta\hbar\omega_i}}{1-e^{-\beta\hbar\omega_i}}, \tag{6}$$

respectively, where $\beta=(k_{\text{B}}T)^{-1}$. The label "$\Gamma$" is retained hereafter to denote that the values have been derived from the Γ-point frequencies only. The total molar values are then

obtained as the sum over modes divided by the number of formula units per cell. The HS-LS Gibbs energy difference is finally obtained as

$$\Delta G^{\Gamma}(T) = \Delta H_{\text{static}} + \Delta E^{\Gamma}_{\text{ZPE}} + \Delta H^{\Gamma}_{\text{vib}}(T) - T\Delta S^{\Gamma}_{\text{vib}}(T) - T\Delta S_{\text{spin}}, \tag{7}$$

in the model excluding orbital entropy, and $\Delta G^{\Gamma}_{\text{orb}}(T) = \Delta G^{\Gamma}(T) - T\Delta S_{\text{orb}}$ in the model including it.

III. COMPUTATIONAL METHOD

All calculations were performed within the CRYSTAL06 linear combinations of atomic-orbitals code.[34] The basis sets used comprise series of contractions of Gaussian-type functions of the form $1s(8)2sp(6)3sp(4)4sp(1)5sp(1)3d(4)4d(1)$ for Fe and Cr; $1s(6)2sp(3)3sp(1)4sp(1)3d(1)$ (corresponding to 6-311G^* in the Pople nomenclature) for C and N; and a Hay-Wadt small-core pseudopotential of valence 9 in combination with a $5sp(3)6sp(1)$ basis for Cs. The Fe, Cr, C, and N sets have all been used in previous studies of Prussian blue and its analogs;[35,36] the Cs set was obtained from the CRYSTAL repository,[37] and has been optimized previously for the Cs^+ state.

Spin-polarized hybrid density functionals of the general form

$$f^{\text{xc}} = \frac{100 - F_0}{100}(f^{\text{x}}_{\text{LSDA}} + 0.9\Delta f^{\text{x}}_{\text{B88}}) + \frac{F_0}{100} f^{\text{x}}_{\text{UHF}} + 0.81 f^{\text{c}}_{\text{LYP}} + 0.19 f^{\text{c}}_{\text{VWN}}, \tag{8}$$

were applied, where x and c denote exchange and correlation contributions, respectively; LSDA, B88, and UHF, the local spin-density approximation, Becke-88,[38] and spin-unrestricted Hartree-Fock exchange potentials, respectively; and VWN and LYP, the Vosko-Wilk-Nusair[39] and Lee-Yang-Parr[40] correlation functionals, respectively. F_0 values of 0%, 10%, 12%, 14%, 16%, 18%, 20%, 30%,…, 90%, and 100% were applied, along with pure UHF exchange. The concentration of points in the range $F_0 = 10-20$ % is motivated by the findings of the previous theoretical studies of SCO complexes and of more general spin transitions discussed above.[18–23] A value $F_0 = 20\%$ (yielding the B3LYP functional) has previously been shown to provide accurate band gaps and dispersions in a wide range of solids[35,41,42] while $F_0 = 35\%$ has been shown to provide accurate magnetic coupling constants in a range of TM compounds.[35,36,43,44] Franchini *et al.* have applied a range of Hamiltonians to MnO and a wider set of multivalent Mn oxides. The PBE0 hybrid functional ($F_0 = 25\%$) was generally recommended for the former material,[45] while a more complex situation arose within the broader study, in that the appropriate Fock exchange admixture was found to be material dependent.[46] The applications of screened hybrid functionals to solids[47] are also worthy of note. The HSE screened hybrid was found to provide a reasonable description of the pressure-induced Mott transition in MnO,[48] of the Jahn-Teller effect in Mn-doped GaN,[49] of the electronic and structural properties of the O vacancy in TiO_2,[50] and of the band gaps and lattice parameters in a wide range of materials.[51] Central to all of these findings is the notion that hybrid functionals offer a systematic means by which to improve the description of materials bearing strongly correlated electrons. Increasing admixture of Fock exchange leads to a more physically realistic localization of the TM d states and opening of the band gap, both due in part to the progressive cancellation of the self-interaction error typical of pure DFT functionals.[42,52]

Initial HS, IS, and LS configurations were obtained by the application of constraints upon the total spin of the cell, and upon the $3d$-orbital occupation at TM sites. However, all total energies and properties derive from converged wave functions obtained after the release of such constraints. Sufficient convergence in total energies was obtained by use of Coulomb and exchange integral series truncation thresholds of 10^{-7}, 10^{-7}, 10^{-7}, 10^{-7}, and 10^{-14} and an $8\times8\times8$ Monkhorst-Pack reciprocal-space mesh, all as described in the code documentation.[34] Optimization convergence tolerances of 10^{-7} atomic units (AU), 0.0003 AU, and 0.0012 AU for total energy, rms force, and rms displacement, respectively, were applied, save in calculations of vibrational frequencies, magnetic coupling constants and JT distortion energies, where tighter tolerances of 10^{-9} AU, 0.00005 AU, and 0.0001 AU, respectively, were used. Tolerances for maximum force and displacement components were set at 1.5 times the respective rms values. Atomic charges and spin populations were obtained from Mulliken analyses of the converged wave functions. Calculations of the zone-center normal vibrational modes proceeded by a series of finite atomic displacements of magnitude 0.005 AU, using lattice symmetry to assist in filling the mass-weighted Hessian matrix.[53,54] IR intensities were obtained for selected Hamiltonians via the atomic dynamical charge tensors[55] computed within the Wannier-Boys localization approach.[56] All calculations adopt a FM alignment of TM spin moments, save where it is noted otherwise.

IV. RESULTS AND DISCUSSION

A. Crystal-field model of the spin excitations

As a guide to the relevant configurations for the DFT calculations, the energies of the various Fe^{II} spin states are explored within a crystal-field Hamiltonian. As in previous studies,[35,57,58] the model due to Kanamori[59] is applied, in which the interaction energies of the d-manifold electrons are expressed in terms of combinations of intra-(U) and interband (U') Coulomb and exchange (J) integrals. Excitation energies relative to the putative $t_{2g}(6)\ e_g(0)$ LS ground state are obtained as

$$\Delta E[\text{LS} \rightarrow \text{IS}_1\{z^2(0)x^2 - y^2(\uparrow)xz(\uparrow\downarrow)yz(\uparrow\downarrow)xy(\uparrow)\}] = \Delta_{\text{CF}} - 3C,$$

$$\Delta E[\text{LS} \rightarrow \text{IS}_2\{z^2(\uparrow)x^2 - y^2(0)xz(\uparrow)yz(\uparrow\downarrow)xy(\uparrow\downarrow)\}] = \Delta_{\text{CF}} + 2B - 3C,$$

$$\Delta E[\text{LS} \rightarrow \text{IS}_3\{z^2(0)x^2 - y^2(\uparrow)xz(\uparrow)yz(\uparrow\downarrow)xy(\uparrow\downarrow)\}] = \Delta_{\text{CF}} + 6B - 3C,$$

$$\Delta E[\mathrm{LS} \rightarrow \mathrm{IS}_4\{z^2(\uparrow)x^2-y^2(0)xz(\uparrow\downarrow)yz(\uparrow\downarrow)xy(\uparrow)\}] = \Delta_{\mathrm{CF}} + 8B - 3C, \quad (9)$$

for the d^6 LS(S=0)→IS(S=1) excitations, where B and C are Racah parameters[60] and Δ_{CF} is the e_g-t_{2g} crystal field splitting energy. The xz and yz orbitals are equivalent under the action of the orbital-dependent U' and J interactions so that their occupancies may be interchanged without effect upon the energy. The IS states shown have been selected from among all possible S=1 configurations on the basis that their respective excitation energies involve only one Δ_{CF} splitting. This is justified by the understanding that Δ_{CF} must exceed the pairing energy in any material manifesting a LS ground state. The Racah parameters are both positive so that the IS_1 configuration emerges as the most stable S=1 state. This configuration is used in the subsequent calculations, and denoted as the IS^L state, "L" indicating the localization of zero occupation in a single orbital.

Applying a similar analysis to the d^6 LS→HS(S=2) excitations yields

$$\Delta E[\mathrm{LS} \rightarrow \mathrm{HS}_1\{z^2(\uparrow)x^2-y^2(\uparrow)xz(\uparrow)yz(\uparrow)xy(\uparrow\downarrow)\}] = 2\Delta_{\mathrm{CF}} - 4B - 7C,$$

$$\Delta E[\mathrm{LS} \rightarrow \mathrm{HS}_2\{z^2(\uparrow)x^2-y^2(\uparrow\downarrow)xz(\uparrow)yz(\uparrow)xy(\uparrow)\}] = 3\Delta_{\mathrm{CF}} - 4B - 7C, \quad (10)$$

where it should be noted that the three distinct $t_{2g}(\uparrow\downarrow)$ configurations lead to energetically equivalent HS_1 states, and the two $e_g(\uparrow\downarrow)$ configurations, to equivalent HS_2 states. The more stable HS_1 configuration is adopted, and denoted as the HS^L state hereafter, "L" in this case indicating the localization of double occupation in one t_{2g} orbital. Interestingly, the excitation energies also reveal the limitations of the simple pairing energy model, in that the combined Coulomb and exchange contribution to the LS→HS^L energy, $(-4B-7C)$, is not an integer multiple of the same for the LS→IS^L energy, $(-3C)$.

JT distortion is anticipated in both spin-excited lattices, the resulting c-axis tetragonal (tet) cell deformations lowering the point symmetry at TM sites from O_h to D_{4h}. As a result, the degenerate O_h t_{2g}-orbitals split into e_g (xz and yz) and b_{2g} (xy) sets, and the O_h e_g orbitals, into $a_{1g}(z^2)$ and b_{1g} (x^2-y^2) sets. However, for simplicity of reference, the present study retains the labeling appropriate to O_h symmetry throughout. Two further HS states are considered: the delocalized (D) $z^2(\uparrow)$ $x^2-y^2(\uparrow)$ $xz(\uparrow 1/3\downarrow)$ $yz(\uparrow 1/3\downarrow)$ $xy(\uparrow 1/3\downarrow)$ configuration in O_h symmetry, and the HS^L configuration, as defined above, in a structure constrained to cubic (cub) geometry in terms of lattice parameters and interatomic distances. Summarizing, the LS, $IS^{L,tet}$, $HS^{L,tet}$, HS^D, and $HS^{L,cub}$ states all carry forward to the subsequent DFT calculations.

B. Static energetics and optimized structures

The optimized structures and relative Fe^{II} spin state energetics obtained in the static limit are presented in Table I and Fig. 2. The main finding is that the experimentally observed LS ground state is stable for $F_0 \leq 18\%$ while a $HS^{L,tet}$ ground state is favored for F_0 values above that range. There is apparently no Hamiltonian within which an $IS^{L,tet}$ ground state is stable. Furthermore, the trends evident in Fig. 2 are qualitatively very similar to those obtained by Reiher for the isolated $Fe(phen)_2(NCS)_2$ complex.[18] The $\Delta H_{\mathrm{static}}$[HS-LS] data obtained in the region F_0=14–16 % are in good agreement with the value +15.7 kJ/mol provided by the previous GGA+U calculations using fixed experimental HS and LS geometries but fall significantly below the value +31.1 kJ/mol resulting from the previous HSE06 hybrid functional calculations.[27] This is an unexpected finding, given that the HSE06 potential incorporates a higher content F_0=25% of Fock exchange, and that the HS-LS splitting apparently decreases with increasing F_0. The larger splitting in the HSE06 calculations is tentatively attributed to the use of fixed experimental geometries, to the sensitivity of the spin state energetics to details of the functionals beyond the Fock exchange content (HSE06 employing the PBE exchange and correlation functionals and short-range Fock exchange only), or to some combination of both effects. Further support for the importance of these points emerges from the fact that the present estimated F_0=25% HS-LS splitting of −24.35 kJ/mol (interpolated linearly between F_0=20% and 30%) differs markedly from the HSE06 value.

Broadly, and in light of the analyses presented in Sec. IV A, the energy differences indicate the progressive dominance of intra-atomic Coulomb and exchange interactions over crystal-field splittings as F_0 increases. This is in keeping with the conclusions drawn from hybrid functional studies of spin excitations in other TM compounds.[18,35,57,58] More specifically, and as discussed previously,[35] $\Delta H_{\mathrm{static}}$[HS-LS] varies directly with the ability of the functionals to adequately represent electron pair correlations, of which one, two, and three manifest within the HS, IS, and LS states, respectively. The UHF method does not account for such interactions, but they are present to varying degrees within most pure DFT functionals, the overall effect being that the LS state is progressively destabilized relative to HS as F_0 increases toward the 100% limit. A qualitatively similar trend emerges for the $\Delta H_{\mathrm{static}}$[IS-LS] splitting, albeit with the lower rate of change with respect to F_0 evident in Fig. 2, the latter due to the fact that this excitation involves the loss of only one pair correlation.

An examination of the nature of the fundamental spin excitation in each Hamiltonian is of interest: these are of the type LS→$HS^{L,tet}$ for $F_0 \leq 18\%$ (save at F_0=0%, where a LS→HS^D excitation is favored); $HS^{L,tet}$→LS for $18\% < F_0 \leq 60\%$; and $HS^{L,tet}$→$IS^{L,tet}$ for $F_0 > 60\%$. Thus, while the IS state never constitutes the ground state of the system, it does become relevant at high admixtures of Fock exchange. It is also found that the $HS^{L,tet}$ and $IS^{L,tet}$ states are variationally unstable at F_0=0%, reverting to the LS configuration upon release of the initial spin constraints. Relative energies at this limit have therefore been approximated by extrapolation of fourth-order polynomial fits to the extant data, as shown in Fig. 2. Similarly, all attempts to obtain a stable HS^D state above F_0=60% result in relaxation into the respective LS configuration. The HS^D-$HS^{L,tet}$ enthalpy difference is found to increase rapidly with F_0, attaining a large value of ap-

TABLE I. Variation with F_0 (%) in the optimized LS, $HS^{L,tet}$, and HS^{D} cell volumes, V (Å^3/molecule), ratio c/a of $HS^{L,tet}$ state lattice constants, and static HS-LS, HS^{D}-$HS^{L,tet}$, and $HS^{L,cub}$-$HS^{L,tet}$ enthalpy differences, ΔH (kJ/mol; superscripts indicate lowest-energy HS state). Experimental values from Refs. 6 and 24, GGA+U and HSE06 values from previous calculations by Wojdeł *et al.* (Ref. 27). † marks ΔH_{static} obtained assuming fixed experimental lattice constants at 100 K and 265 K for LS and HS states, respectively.

F_0	V(LS)	$V(HS^{L,tet})$	$V(HS^{D})$	$c/a(HS^{L,tet})$	ΔH_{static}(HS-LS)	ΔH (HS^{D}-$HS^{L,tet}$)	ΔH_{JT} ($HS^{L,cub}$-$HS^{L,tet}$)
0	276.27		308.24		$+94.58^{D}$		
10	280.00	316.43	308.37	1.0024	$+46.17^{L,tet}$	+31.73	+0.043
12	280.76	317.01	308.37	1.0019	$+34.99^{L,tet}$	+41.78	+0.029
14	281.51	317.54	308.35	1.0014	$+24.59^{L,tet}$	+50.20	+0.019
16	282.20	318.01	308.31	1.0010	$+13.97^{L,tet}$	+61.75	+0.013
18	282.94	318.42	308.24	1.0006	$+4.11^{L,tet}$	+72.02	+0.009
20	283.60	318.78	308.15	1.0004	$-2.28^{L,tet}$	+81.90	+0.008
30	286.74	320.11	307.44	0.9991	$-46.42^{L,tet}$	+132.74	+0.022
40	289.27	320.72	306.29	0.9983	$-80.61^{L,tet}$	+181.65	+0.038
50	291.03	321.02	304.80	0.9978	$-108.78^{L,tet}$	+227.70	+0.057
60	292.51	321.04	303.11	0.9975	$-132.74^{L,tet}$	+270.59	+0.075
70	293.28	320.85		0.9973	$-153.71^{L,tet}$		+0.089
80	294.03	320.52		0.9971	$-170.42^{L,tet}$		+0.106
90	294.52	320.12		0.9971	$-187.12^{L,tet}$		+0.110
100	294.80	319.52		0.9970	$-202.77^{L,tet}$		+0.116
UHF	318.59	343.78		0.9955	$-309.82^{L,tet}$		+0.196
GGA+U (Ref. 27)	277.98	306.26			$+15.73^{\dagger}$		
HSE06 (Ref. 27)					$+31.07^{\dagger}$		
Expt.	$275.58^{180\ K}$ (Ref. 6), $276.18^{204\ K}$ (Ref. 24)	$306.95^{280\ K}$ (Ref. 6), $307.23^{268\ K}$ (Ref. 24)					

proximately 271 kJ/mol at the HS^{D} stability limit. It is clear from this that the inclusion of orbital relaxation is a key factor determining the relative spin state energies in Hamiltonians containing Fock exchange. Calculations on the isolated Fe^{II} ion provide quantitatively similar results, indicating that the HS^{D}-HS^{L} splitting is due to intra-atomic interactions, but such effects lie beyond the scope of the simple crystal-field model presented earlier.

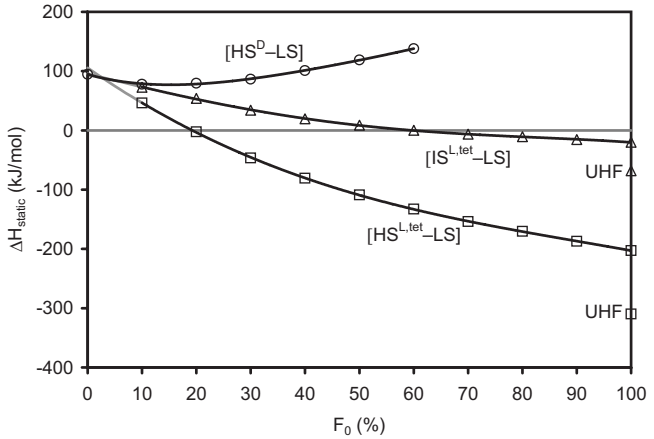

FIG. 2. The variation with F_0 (%) in the energies relative to the optimized LS lattice of the optimized cubic HS^{D}, tetragonal HS^{L}, and tetragonal IS^{L} states. Extrapolations of the $HS^{L,tet}$-LS and $IS^{L,tet}$-LS curves are shown in the F_0 range from 0% to 10%.

In contrast, the enthalpy differences, ΔH_{JT}, separating the $HS^{L,cub}$ and $HS^{L,tet}$ states are very small (of order 0.2 kJ/mol or less), in keeping with the understanding that degenerate t_{2g}-orbital occupation in octahedral symmetry typically leads to a weak JT effect. In fact, the distortion energies are sufficiently small relative to the thermal energy at $T_{1/2}$ and above that a dynamical JT effect might be anticipated. To a first approximation, the onset of such disorder is expected when $T\Delta S_{orb}$ (ΔS_{orb} amounting to 9.13 J/mol K in the present material) exceeds the associated enthalpy cost, ΔH_{JT}. The orbital occupation at Fe^{II} sites then fluctuates over the degenerate $e_g^2 t_{2g}^2 xz(\uparrow\downarrow)$, $e_g^2 t_{2g}^2 yz(\uparrow\downarrow)$, and $e_g^2 t_{2g}^2 xy(\uparrow\downarrow)$ HS_1-type configurations discussed in Sec. IV A. The calculations support the presence of such disorder, yielding ΔH_{JT} values amounting to no more than one tenth the value of $T_{1/2}\Delta S_{orb}$ at the mean experimental crossover temperature. The most apparent effect would be to create a HS state lattice appearing cubic to experimental techniques averaging over sufficiently long distances or time scales. X-ray diffraction studies of $CsFe^{II}[Cr^{III}(CN)_6]$ reveal such a structure above $T_{1/2}$, finding no evidence of a static JT distortion.[6] A number of further points arise in relation to this disorder. First, the relative energies firmly establish that the dynamical JT state must involve fluctuations over distinct HS_1-type configurations, rather than the higher symmetry state of average occupation represented by the HS^{D} configuration. Second, the presence of a dynamical JT effect in the HS state would seem to require the inclusion of ΔS_{orb} in the SCO thermodynamic

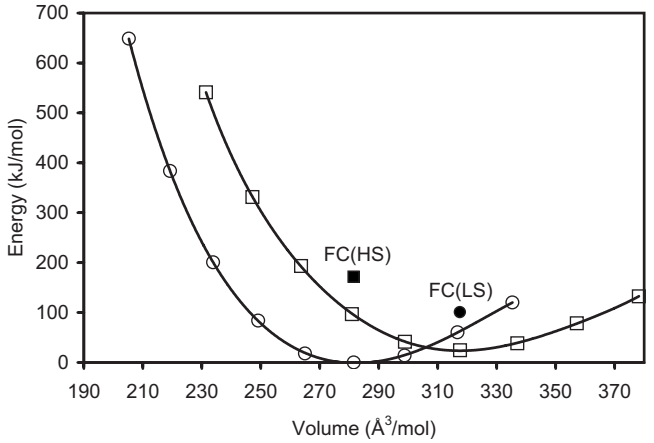

FIG. 3. The variations with volume in the energies relative to the optimized LS lattice of the LS (○) and tetragonal HS^L (□) lattices for $F_0=14\%$. Also shown are the relative energies of the corresponding Franck-Condon excited states (FC, filled symbols), i.e., the HS state within the optimized LS geometry and vice versa. Lines show fourth-order polynomial fits.

model. Third, it is noted that the ΔH_{JT} values obtained here relate to a cooperative distortion of the whole lattice. Future supercell simulations will consider the effects of more localized distortions.

Examining optimized structures (Table I), it is clear that the LS→HS transition always occurs with an increase in molar volume. The best overall agreement with the experimental LS and HS volumes comes from the $F_0=0\%$ method, though all functionals provide volume increases that are reasonably close to both the experimental[6,24] and the previous optimized GGA+U values.[27] As might be anticipated from simple ligand field arguments, the structural effect is dominated by the elongation of Fe—N bonds arising due to the occupation of antibonding Fe^{II} e_g orbitals. The fractional changes in Cr—C and C≡N distances are much smaller, amounting to no more than approximately 4% and 2%, respectively, of the fractional change in the comparable mean Fe—N distance, all relative to the corresponding bond lengths in the LS state. The mean Fe—N bond elongation across the transition varies from 0.14 Å in the UHF method, to 0.20 Å at $F_0=0\%$, bracketing the experimental values in the approximate range 0.17–0.18 Å (Ref. 24) and the value 0.17 Å obtained from the previous GGA+U calculations.[27] The HS state lattice constant ratios, c/a, remain close to unity across the range of functionals, although a crossover from relative elongation to contraction along the c axis occurs in the range $20\%<F_0<30\%$, ΔH_{JT} approaching a minimum in the same region.

A representative set of LS and HS state energy-volume curves obtained within the $F_0=14\%$ functional are shown in Fig. 3. Polynomial fits permit for the determination of the respective bulk moduli, K_0, via

$$K_0 = V_0 \left.\frac{\partial^2 E}{\partial V^2}\right|_{V_0}. \tag{11}$$

The fourth-order functions shown in Fig. 3 yield values of approximately 60 GPa and 51 GPa for LS and $HS^{L,tet}$ states, respectively. Similar values were obtained across the range $0\% \le F_0 \le 18\%$ within which the LS ground state is favored. Thus, it emerges that occupation of the Fe^{II} e_g orbitals leads not only to increased Fe—N bond lengths but also to increased lattice compressibility. Both effects are relevant to the piezomagnetic properties displayed by this material.[7] However, further comparisons are hampered by the fact that experimental bulk moduli are presently unavailable.

Figure 3 also shows the relative energies of the LS→HS and HS→LS Franck-Condon (FC) states, i.e., the spin-excited states obtained with lattice fixed as in the appropriate optimized initial state. Values of approximately 172 kJ/mol and 76 kJ/mol emerge for LS→HS and HS→LS transitions, respectively, placing such states substantially higher in energy than the corresponding optimized excited states at equivalent volume. The previous GGA+U and HSE06 calculations, using fixed low- and high-temperature experimental structures, provide similar values of approximately 163–167 kJ/mol for the FC LS→HS energy, but the FC HS→LS excitation is placed much lower at approximately 17–18 kJ/mol.[27] At least part of this discrepancy may be ascribed to the modest overestimation relative to experiment of the HS state volume in the present $F_0 \ge 10\%$ optimizations. Furthermore, while it is noted that such energies relate directly to optical absorption, the transitions in the present material are forbidden by both the parity- and spin-selection rules, so that optical excitation is expected to be very inefficient.

C. Thermodynamic parameters and phonon frequencies

Lattice-dynamics calculations, as outlined in Sec. II, were pursued for the LS and HS states in all Hamiltonians within which a LS ground state is favored. Values of the interaction constant, Φ, at $\gamma=1/2$ were also obtained for each functional from the static total energies of fully optimized bimolecular supercells (vectors $\mathbf{a}_{SC}=\mathbf{b}_{prim}+\mathbf{c}_{prim}$, $\mathbf{b}_{SC}=\mathbf{a}_{prim}+\mathbf{c}_{prim}$, $\mathbf{c}_{SC}=\mathbf{a}_{prim}+\mathbf{b}_{prim}$; prim denoting the rhombohedral primitive cell) containing one HS and one LS Fe site. The molar excess enthalpy of mixing $H_{mix}=\frac{1}{2}[E_{SCell}-E_{LS}-E_{HS}]$ may then be equated with the term $\Phi\gamma(1-\gamma)$ appearing in Eq. (2), yielding the interaction constant directly. It is emphasized that the Φ values obtained in this way represent preliminary estimates: a fuller treatment would entail averaging over multiple supercell expansions and the inclusion of vibrational contributions.

Table II presents the thermodynamic parameters derived from the calculations while Fig. 4 shows the variations in the Gibbs energy differences ΔG^{Γ} and ΔG^{Γ}_{orb} with temperature. It is clear that the pure DFT approach overestimates the SCO transition temperature, the $T^{\Gamma}_{1/2}$ values falling thereafter as F_0 is increased, in close correlation with the trend in ΔH_{static}. Figure 4 further reveals that the $\Delta G^{\Gamma}(T)$ and $\Delta G^{\Gamma}_{orb}(T)$ curves obtained from each functional are all of similar form, the only substantial difference arising in regard to their zero-temperature intercepts, $\Delta G^{\Gamma}(0)=\Delta G^{\Gamma}_{orb}(0)=\Delta H_{static}+\Delta E^{\Gamma}_{ZPE}$. Given that the ZPE contribution is of a similar magnitude in all functionals, it can be concluded that the wide range in computed $T^{\Gamma}_{1/2}$ values is due mainly to the variations in

TABLE II. Variation with F_0 (%) in the static enthalpy difference, ΔH_{static} (kJ/mol), net zero-point energy difference, $\Delta E^{\Gamma}_{\text{ZPE}}$ (kJ/mol), net vibrational enthalpy difference at the transition temperature, $\Delta H^{\Gamma}_{\text{vib}}(T^{\Gamma}_{1/2})$ (kJ/mol), net vibrational entropy difference at the transition temperature, $\Delta S^{\Gamma}_{\text{vib}}(T^{\Gamma}_{1/2})$ (J/mol K), transition temperature, $T^{\Gamma}_{1/2}$ (K), interaction constant, $\Phi(\gamma=1/2)$(kJ/mol), and critical interaction constant, $\Phi_C=2RT_{1/2}$ (kJ/mol). Δ denotes HS-LS difference; orb, value in model including orbital entropy. Experimental $T_{1/2}$ values from Ref. 6, experimental estimates of Φ_C based on the latter values. Parameters obtained assuming access only to IR- or Raman-active modes and $T^{\Gamma}_{1/2}=206.9$ K are also shown for $F_0=14\%$. d indicates value derived assuming unity for all mode degeneracies.

F_0	ΔH_{static}	$\Delta E^{\Gamma}_{\text{ZPE}}$	$\Delta H^{\Gamma}_{\text{vib}}(T^{\Gamma}_{1/2})$	$\Delta S^{\Gamma}_{\text{vib}}(T^{\Gamma}_{1/2})$	$T^{\Gamma}_{1/2}$	$\Phi(\gamma=1/2)$	$\Phi_C=2RT_{1/2}$
0	+94.58	−11.71	+9.95, +9.76$^{\text{orb}}$	+66.50, +66.30$^{\text{orb}}$	1162.1, 1042.7$^{\text{orb}}$	12.18	19.32, 17.34$^{\text{orb}}$
10	+46.17	−13.34	+9.19, +8.81$^{\text{orb}}$	+76.46, +75.60$^{\text{orb}}$	467.7, 424.4$^{\text{orb}}$	3.02	7.78, 7.06$^{\text{orb}}$
12	+34.99	−13.10	+7.78, +7.30$^{\text{orb}}$	+70.35, +68.94$^{\text{orb}}$	354.4, 319.3$^{\text{orb}}$	3.73	5.89, 5.31$^{\text{orb}}$
14	+24.59	−12.67	+5.60, +5.00$^{\text{orb}}$	+61.99, +59.27$^{\text{orb}}$	232.4, 206.9$^{\text{orb}}$	3.84	3.86, 3.44$^{\text{orb}}$
14 IR only		+3.25, +27.99$^{\text{d}}$	+9.13$^{\text{orb}}$ +8.63$^{\text{orb,d}}$	+91.31$^{\text{orb}}$, +81.68$^{\text{orb,d}}$			
14 Raman only		+2.19, +42.93$^{\text{d}}$	+9.39$^{\text{orb}}$, +9.14$^{\text{orb,d}}$	+93.21$^{\text{orb}}$, +85.14$^{\text{orb,d}}$			
16	+13.97	−12.79	+0.59, +0.39$^{\text{orb}}$	+20.75, +16.50$^{\text{orb}}$	52.0, 40.4$^{\text{orb}}$	3.02	0.86, 0.67$^{\text{orb}}$
18	+4.11	−13.15					
Expt.					211–238 (Ref. 6)		3.51–3.96

ΔH_{static}. However, $\Delta E^{\Gamma}_{\text{ZPE}}$ does play an important role at $F_0=18\%$, wherein it suffices to stabilize a HS ground state, eliminating any possibility of a temperature-driven SCO. The $\Delta H^{\Gamma}_{\text{vib}}(T^{\Gamma}_{1/2})$ and $\Delta S^{\Gamma}_{\text{vib}}(T^{\Gamma}_{1/2})$ values shown in Table II vary markedly, due mainly to the large range in the associated $T^{\Gamma}_{1/2}$ values. Moreover, the SCO thermodynamics including and excluding ΔS_{orb} are, in most cases, very similar. Inclusion of the latter leads to decreases in transition temperature of approximately 10–20 % across the range of functionals, and to relative reductions in $\Delta H^{\Gamma}_{\text{vib}}(T^{\Gamma}_{1/2})$ and $\Delta S^{\Gamma}_{\text{vib}}(T^{\Gamma}_{1/2})$ that are small at the pure DFT limit, but grow progressively larger as F_0 is increased.

The $T^{\Gamma}_{1/2}$ values obtained at $F_0=14\%$ are in excellent agreement with the experimental range,[6,7] in keeping with the suggestions of previous studies that functionals in the region $F_0\approx 15\%$ provide reliable relative spin state energetics.[18,22,23] However, it is recalled that the occurrence of two experimental values is a consequence of hysteresis so that it may be more appropriate to compare the computed $T^{\Gamma}_{1/2}$ values with the experimental average at 225 K. The $F_0=14\%$ functional yields total enthalpy differences across the transition of 17.5 kJ/mol and 16.9 kJ/mol for models excluding and including orbital entropy, respectively; vibrational entropy changes of 62.0 J/mol K and 59.3 J/mol K, respectively; and total entropy changes of 75.4 J/mol K and 81.8 J/mol K, respectively. The latter values lie at the upper end of the broad range from 35–80 J/mol K typically quoted for octahedral Fe^{II} complexes.[13] Vibrations contribute 82% of the total transition entropy in the model excluding ΔS_{orb} and 72% in the model including it, bearing out the discussion of the relative importance of the electronic and vibrational contributions presented in Sec. II.

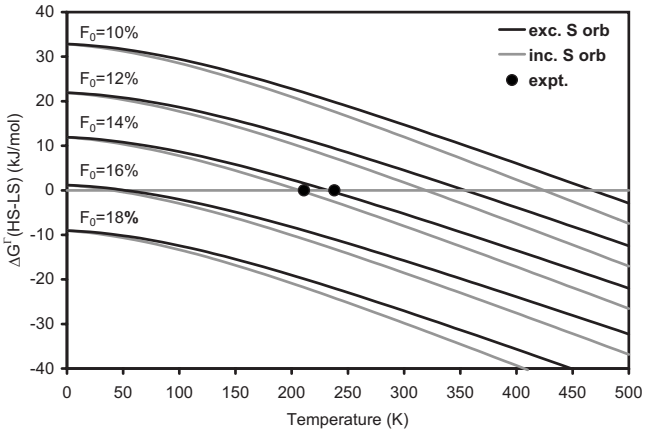

FIG. 4. The variations with temperature in the Gibbs energy difference separating $HS^{L,tet}$ and LS forms, as obtained from Γ-point lattice-dynamics calculations in the $F_0=10\%$, 12%, 14%, 16%, and 18% functionals. Curves for Gibbs energies including and excluding ΔS_{orb} are shown. Filled circles mark experimental values (Ref. 6).

Table II also compares the interaction constants obtained from the supercell calculations with the respective critical values $\Phi_C=2RT_{1/2}$ separating continuous and discontinuous transitions. Mindful of the approximations involved, transitions with a range of characters are predicted. The constants at $F_0=0\%$, 10%, and 12% lie well below the respective Φ_C values, indicating gradual and continuous SCO, while those at $F_0=14\%$ and 16% are in the region of or greater than Φ_C, indicating discontinuous transitions with the potential for hysteresis. The latter two results concur with the experimental observation that SCO in $CsFe[Cr(CN)_6]$ is abrupt in onset and hysteretic.[6,7] No obvious reason emerges for the much larger Φ value obtained at the pure DFT limit. Despite the clear differences in HS^{D} and $HS^{L,tet}$ orbital occupations, the optimized Fe—Fe distances in the mixed HS+LS supercell at $F_0=0\%$ are very similar to those obtained with other functionals. Further study of this point is required, perhaps with extension to more conventional SCO solids.

Representative sets of mode wave numbers and associated thermodynamic quantities obtained from the $F_0=14\%$ lattice-dynamics calculations are presented in Tables III and IV for LS and HS states, respectively. Also shown are the irreducible representations and assignments of the modes, their IR and Raman activities, and IR intensities. The corre-

TABLE III. Wave number, $\tilde{\nu}$ (cm^{-1}), irreducible representation, IR activity (A=active, I=inactive), IR intensity (km/mol), Raman activity, zero-point energy, E^{Γ}_{ZPE} (J/mol), enthalpy, $H^{\Gamma}_{vib}(T^{\Gamma}_{1/2})$ (J/mol), entropy $S^{\Gamma}_{vib}(T^{\Gamma}_{1/2})$ (J/mol K), and assignment of the LS state normal modes in the F_0=14% Hamiltonian. Thermodynamic quantities shown take account of the mode degeneracies. OOP denotes out-of-plane motion; IP, in-plane motion; def, deformation; symm, symmetric stretch; asymm, asymmetric stretch; x_1, x_2, y_1, y_2, z_1, and z_2, the labels of the CN^- ligands; +/− signs, the relative phase of ν(CN) motion; orb, value in model including orbital entropy.

Modes	$\tilde{\nu}$	Irrep.	IR (Intensity)	Raman	E^{Γ}_{ZPE}	$H^{\Gamma}_{vib}(T^{\Gamma}_{1/2})$	$S^{\Gamma}_{vib}(T^{\Gamma}_{1/2})$	Assignment
1–3	−4.04	F_2	A (0.00)	A				Acoustic
4–6	61.88	F_2	A (34.54)	A	1110.36	4757.21, 4129.82^{orb}	49.03, 46.17^{orb}	Cs translation
7–9	98.54	F_1	I	I	1768.17	4207.35, 3593.00^{orb}	37.65, 34.85^{orb}	FeN_4 and CrC_4 counter-rotation
10–12	244.65	F_1	I	I	4390.04	2474.84, 1959.36^{orb}	16.84, 14.49^{orb}	FeN_4 and CrC_4 OOP tetrahedral def.
13–15	254.90	F_2	A (91.78)	A	4573.86	2378.81, 1872.31^{orb}	16.00, 13.69^{orb}	FeN_4 and CrC_4 OOP pyramidal def.+ν(CrC)+ν(FeN)
16–18	290.48	F_2	A (0.30)	A	5212.38	2068.54, 1594.42^{orb}	13.42, 11.26^{orb}	FeN_4 and CrC_4 IP def.
19–21	321.61	F_2	A (5.05)	A	5770.89	1825.32, 1380.61^{orb}	11.52, 9.49^{orb}	FeN_4 and CrC_4 OOP pyramidal def.
22–24	340.32	F_1	I	I	6106.73	1690.95, 1264.21^{orb}	10.51, 8.57^{orb}	FeN_4 and CrC_4 corotation
25–27	441.16	F_1	I	I	7916.20	1103.19, 772.50^{orb}	6.43, 4.92^{orb}	FeN_4 and CrC_4 OOP tetrahedral def.
28–29	449.35	E	I	A	5375.39	709.65, 494.19^{orb}	4.12, 3.14^{orb}	Asymm. ν(CrC)+ν(FeN)
30–32	466.62	F_2	A (0.67)	A	8373.01	986.69, 679.13^{orb}	5.67, 4.27^{orb}	FeN_4 and CrC_4 IP def.
33	476.17	A	I	A	2848.16	315.28, 215.60^{orb}	1.80, 1.35^{orb}	Symm. ν(CrC)+ν(FeN)
34–36	494.03	F_2	A (393.34)	A	8864.96	873.55, 590.07^{orb}	4.96, 3.67^{orb}	FeN_4 and CrC_4 OOP pyramidal def.+ν(CrC)+ν(FeN)
37–39	502.04	F_2	A (22.43)	A	9008.55	842.78, 566.15^{orb}	4.77, 3.51^{orb}	FeN_4 and CrC_4 OOP pyramidal def.+ν(CrC)+ν(FeN)
40	2207.95	A	I	A	13206.46	0.03, 0.01^{orb}	0.00, 0.00^{orb}	ν(CN)$[x_1+x_2+y_1+y_2+z_1+z_2]$
41–43	2222.17	F_2	A (201.30)	A	39874.53	0.08, 0.02^{orb}	0.00, 0.00^{orb}	ν(CN)$[x_1-x_2]$/ ν(CN)$[y_1-y_2]$ / ν(CN)$[z_1-z_2]$
44–45	2224.28	E	I	A	26608.24	0.06, 0.01^{orb}	0.00, 0.00^{orb}	ν(CN)$[x_1+x_2+y_1+y_2-z_1-z_2]$ / ν(CN)$[x_1+x_2-y_1-y_2]$

sponding mode eigenvectors are presented in the Supplementary Material.[61] Examination of the latter often indicates mixed character; the assignments listed in the tables represent the dominant site motions determined by visual inspection. While mode coupling of this type complicates the comparison of the LS and HS spectra, some specific insights may be obtained. The thermodynamic model including ΔS_{orb} is adopted hereafter to simplify the discussion. The breakdown of contributions to $\Delta S^{\Gamma}_{vib}(T^{\Gamma}_{1/2})$ by dominant mode motion is,

Cs translations	+10.6,
FeN_4 and CrC_4 counter-rotations	+13.2,
OOP tetrahedral deformations	+11.9,
OOP pyramidal deformations	+13.4,
IP deformations	+6.3,
FeN_4 and CrC_4 corotations	+2.1,
Asymmetric and symmetric ν(FeN) and ν(CrC)	+1.9,
ν(CN)	0.0 J/mol K.

However, many of the modes display substantial ν(FeN) and ν(CrC) character so that the metal-ligand stretching contribution is likely greater than is apparent here. More than half of $\Delta S^{\Gamma}_{vib}(T^{\Gamma}_{1/2})$ derives from the nine lowest, nonacoustic modes possessing wave numbers of 250 cm^{-1} or lower. It is difficult to conceive of an isolated cluster approach capable of accurately representing the lower six of these modes, emphasizing the importance of a solid-state lattice-dynamics approach for the present material. The contribution of the Cs translational (or "rattling") modes are of particular interest, for the mode softening here derives chiefly from the lattice expansion in the HS state, rather than from any direct reduction in bond strength; the same likely also applies for the FeN_4 and CrC_4 rotational modes.

The effects of the spectroscopic selection rules upon the apparent SCO thermodynamics are also of interest. Separate analyses follow for the cases that the mode degeneracies can and cannot be experimentally determined, being set to unity in the latter case. It is also assumed that even the weakest IR- or Raman-active absorptions may be resolved. Summing over only the IR-active modes with correct degeneracies yields ΔE^{Γ}_{ZPE}, $\Delta H^{\Gamma}_{vib}(T^{\Gamma}_{1/2})$, and $\Delta S^{\Gamma}_{vib}(T^{\Gamma}_{1/2})$ values of approximately +3.3 kJ/mol, +9.1 kJ/mol, and +91.3 J/mol K, respectively; and similarly over the Raman-active modes, +2.2 kJ/mol, +9.4 kJ/mol, and +93.2 J/mol K, respectively, all as shown in Table II. The thermodynamic parameters assuming access to both IR and Raman frequencies are identical to the Raman-only values, for there are no modes in either spin state that are both IR active and Raman silent. Summations with degeneracies set to unity yield only relatively minor changes in $\Delta H^{\Gamma}_{vib}(T^{\Gamma}_{1/2})$ and $\Delta S^{\Gamma}_{vib}(T^{\Gamma}_{1/2})$, and

TABLE IV. Wave number, $\tilde{\nu}$ (cm^{-1}), irreducible representation, IR activity (A=active, I=inactive), IR intensity (km/mol), Raman activity, zero-point energy, E^{Γ}_{ZPE} (J/mol), enthalpy, $H^{\Gamma}_{vib}(T^{\Gamma}_{1/2})$ (J/mol), entropy $S^{\Gamma}_{vib}(T^{\Gamma}_{1/2})$ (J/mol K), and assignment of the $HS^{L,tet}$ state normal modes in the F_0=14% Hamiltonian. Thermodynamic quantities shown take account of the mode degeneracies. OOP denotes out-of-plane motion; IP, in-plane motion; def, deformation; symm, symmetric stretch; asymm, asymmetric stretch; x_1, x_2, y_1, y_2, z_1, and z_2, the labels of the CN^- ligands; +/− signs, the relative phase of ν(CN) motion; orb, value in model including orbital entropy; one Cartesian axis (e.g., x) indicates axis of motion; two Cartesian axes (e.g., xy) indicate plane of motion.

Modes	$\tilde{\nu}$	Irrep.	IR (Intensity)	Raman	E^{Γ}_{ZPE}	$H^{\Gamma}_{vib}(T^{\Gamma}_{1/2})$	$S^{\Gamma}_{vib}(T^{\Gamma}_{1/2})$	Assignment
1–2	−3.91	E	A (0.00)	A				Acoustic
3	−3.89	B_2	A (0.00)	A				Acoustic
4	38.09	B_2	A (13.97)	A	227.85	1713.38, 1502.46^{orb}	20.35, 19.38^{orb}	Cs translation (z)
5–6	41.48	E	A (28.40)	A	496.20	3389.58, 2968.15^{orb}	39.28, 37.36^{orb}	Cs translation (x/y)
7–8	52.05	E	A (0.13)	A	622.65	3275.30, 2855.36^{orb}	35.53, 33.62^{orb}	FeN_4 and CrC_4 counter-rotation (x/y)
9	69.78	A_2	I	I	417.37	1544.87, 1336.52^{orb}	15.36, 14.41^{orb}	FeN_4 and CrC_4 counter-rotation (z)
10	144.62	A_2	I	I	865.04	1194.64, 997.83^{orb}	9.51, 8.61^{orb}	FeN_4 and CrC_4 OOP tetrahedral def. (z)
11–12	162.20	E	A (20.50)	A	1940.33	2243.64, 1857.45^{orb}	17.24, 15.48^{orb}	FeN_4 and CrC_4 OOP tetrahedral def. (x/y)
13–14	206.54	E	A (42.40)	A	2470.72	1906.57, 1541.85^{orb}	13.63, 11.97^{orb}	FeN_4 and CrC_4 OOP pyramidal def.+ν(CrC)+ν(FeN)(x/y)
15	209.31	B_2	A (177.95)	A	1251.94	943.45, 761.82^{orb}	6.72, 5.89^{orb}	FeN_4 and CrC_4 OOP pyramidal def.+ν(CrC)+ν(FeN)(z)
16–17	222.54	E	A (3.35)	A	2662.18	1795.18, 1439.06^{orb}	12.56, 10.93^{orb}	FeN_4 and CrC_4 IP def. (xz/yz)
18	227.32	B_2	A (5.13)	A	1359.66	881.48, 704.74^{orb}	6.13, 5.32^{orb}	FeN_4 and CrC_4 OOP pyramidal def.+ν(FeN)(z)
19	232.45	B_2	A (3.59)	A	1390.34	864.44, 689.13^{orb}	5.97, 5.17^{orb}	FeN_4 and CrC_4 IP def. (x/y)
20–21	243.68	E	A (115.70)	A	2915.12	1656.04, 1311.83^{orb}	11.28, 9.72^{orb}	FeN_4 and CrC_4 OOP pyramidal def. (x/y)
22–23	297.82	E	A (0.00)	A	3562.75	1339.25, 1027.75^{orb}	8.63, 7.21^{orb}	FeN_4 and CrC_4 corotation (x/y)
24	305.55	A_2	I	I	1827.60	649.20, 495.88^{orb}	4.15, 3.45^{orb}	FeN_4 and CrC_4 corotation (z)
25	369.09	A_2	I	I	2207.66	500.27, 367.27^{orb}	3.05, 2.44^{orb}	FeN_4 and CrC_4 OOP tetrahedral def. (z)
26–27	373.55	E	A (134.61)	A	4468.59	982.04, 718.90^{orb}	5.96, 4.76^{orb}	FeN_4 and CrC_4 OOP tetrahedral def.+ν(CrC)+ν(FeN)(x/y)
28	376.16	B_2	A (226.71)	A	2249.94	485.66, 354.93^{orb}	2.94, 2.35^{orb}	FeN_4 and CrC_4 OOP pyramidal def.+ν(CrC)+ν(FeN)(z)
29	377.79	B_1	I	A	2259.69	482.34, 352.13^{orb}	2.92, 2.33^{orb}	Asymm. ν(CrC) and ν(FeN)
30	379.32	A_1	I	A	2268.83	479.25, 349.53^{orb}	2.90, 2.31^{orb}	Asymm. ν(CrC) and ν(FeN)
31–32	386.84	E	A (175.64)	A	4627.56	928.60, 673.98^{orb}	5.59, 4.43^{orb}	FeN_4 and CrC_4 OOP pyramidal def.+ν(CrC)+ν(FeN)(x/y)
33–34	413.05	E	A (1.26)	A	4941.16	830.51, 592.53^{orb}	4.92, 3.83^{orb}	FeN_4 and CrC_4 IP def. (xz/yz)
35	419.68	B_2	A (0.59)	A	2510.25	403.58, 286.68^{orb}	2.38, 1.85^{orb}	FeN_4 and CrC_4 IP def. (xy)
36	429.70	A_1	I	A	2570.14	386.51, 272.73^{orb}	2.27, 1.75^{orb}	Symm. ν(CrC) and ν(FeN)
37	471.18	B_2	A (124.72)	A	2818.26	322.34, 221.18^{orb}	1.85, 1.39^{orb}	FeN_4 and CrC_4 OOP pyramidal def.+ν(CrC)+ν(FeN)(z)
38–39	475.09	E	A (240.79)	A	5683.36	633.60, 433.59^{orb}	3.63, 2.72^{orb}	FeN_4 and CrC_4 OOP pyramidal def.+ν(CrC)+ν(FeN)(x/y)
40–41	2215.34	E	A (6.42)	A	26501.38	0.06, 0.01^{orb}	0.00, 0.00^{orb}	ν(CN)[x_1-x_2]/ ν(CN)[y_1-y_2]
42	2216.05	B_1	I	A	13254.90	0.03, 0.01^{orb}	0.00, 0.00^{orb}	ν(CN)[$x_1+x_2-y_1-y_2$]
43	2219.34	A_1	I	A	13274.61	0.03, 0.01^{orb}	0.00, 0.00^{orb}	ν(CN)[$x_1+x_2+y_1+y_2-z_1-z_2$]
44	2229.58	B_2	A (171.25)	A	13335.86	0.03, 0.00^{orb}	0.00, 0.00^{orb}	ν(CN)[z_1-z_2]
45	2232.43	A_1	I	A	13352.86	0.03, 0.00^{orb}	0.00, 0.00^{orb}	ν(CN)[z_1+z_2]

large increases in ΔE^{Γ}_{ZPE}. Taking the results together, it is clear that the thermodynamic parameters derived from the partial sets of modes differ markedly from the complete set values, emphasizing the difficulties inherent to the determination of such quantities from spectroscopies limited by selection rules. On this basis, application of the inelastic neutron-scattering technique might be preferred.

The experimental spectra reported for $CsFe[Cr(CN)_6]$ are limited to IR frequencies in the ν(CN) region.[6,7] It is found that the experimental stretches at 2156 cm^{-1} and 2163 cm^{-1} in the LS and HS states, respectively,[6] compare reasonably well with $F_0=14\%$ values of 2222 cm^{-1} (F_2 symmetry) and 2230 cm^{-1} (B_2 symmetry), respectively, particularly in regard to the HS-LS difference. The latter modes were selected on the basis of their large computed IR intensities. Interestingly, the lattice-dynamics calculations also reveal the presence in the HS state IR spectrum of a weak ν(CN) E-symmetry mode approximately 15 cm^{-1} below the strong absorption. A feature analogous to this is observed in the experimental HS spectrum, where it was attributed to the presence of minority Fe(LS)-NC-Cr configurations.[7] It is suggested that this assignment is incorrect, and that this weak peak is, in fact, intrinsic to the HS state.

V. CONCLUSIONS

The present study comprises a detailed investigation of thermal SCO in the $CsFe[Cr(CN)_6]$ Prussian blue analog, including a lattice-dynamics treatment of the key thermodynamic parameters driving the cooperative transition. The main finding is that the static and dynamical enthalpy and entropy differences derived from a solid-state hybrid density-functional approach with a Fock exchange content $F_0=14\%$, in combination with a simple thermodynamical model for SCO, leads to transition temperatures in excellent agreement with the experimental range. The superior performance of hybrid functionals in this F_0 region bears out the findings of previous studies of the spin excitations in a range of isolated complexes.[18–23] The variations in spin state splitting energies with F_0 may be understood in terms of the extent to which the various functionals capture electron pair correlations. The calculations effectively complement the experimental studies, yielding detailed insights into the transition thermodynamics and equation-of-state parameters. Other important findings include:

(i) the fundamental Fe^{II} spin excitations of the system are of type $LS \rightarrow HS^{D}$ for $F_0=0\%$, $LS \rightarrow HS^{L,tet}$ for $10\% \leq F_0 \leq 18\%$, $HS^{L,tet} \rightarrow LS$ for $18\% < F_0 \leq 60\%$, and $HS^{L,tet} \rightarrow IS^{L,tet}$ for $F_0 > 60\%$.

(ii) Estimates of the lattice distortion energy ΔH_{JT} associated with the JT effect in the HS Fe^{II} $e_g^2 t_{2g}^4$ configuration provide values that are small relative to the thermal energy at $T_{1/2}$ and above. This is interpreted to indicate the likely presence of a dynamic JT effect in the HS state, in keeping with the experimental assignment of cubic symmetry for this phase.

(iii) Essentially all of the functionals provide reasonable values for the increase in molar volume associated with the $LS \rightarrow HS$ transition, though ΔV at $F_0=0\%$ lies closest to experiment. The bulk moduli in the HS state are found to be approximately 15% lower than in the LS state.

(iv) The $\Delta G^{\Gamma}(T)=G^{\Gamma}_{HS}(T)-G^{\Gamma}_{LS}(T)$ curves are of similar form in all relevant Hamiltonians $0\% \leq F_0 \leq 18\%$, the only significant difference arising in relation to their zero-temperature intercepts, driven chiefly by the variation in ΔH_{static} with F_0. It is also clear that the choice of whether to include or exclude the entropy associated with orbital degeneracy in the $HS^{L,tet}$ state results in only modest changes to the relevant thermodynamic parameters.

(v) Vibrations contribute the dominant fraction of the transition entropy, and more than half of ΔS_{vib} arises from modes with wave numbers of 250 cm^{-1} or less, the majority of which would not be straightforwardly representable within a cluster approach. Application of the spectroscopic selection rules leads to thermodynamic parameters differing markedly from those obtained with the full sets of frequencies, indicating that the derivation of SCO thermodynamics directly from IR or Raman spectroscopy may lead to significant error. Similar difficulties are anticipated in other SCO materials.

(vi) The computed ν(CN) stretching modes displaying significant IR intensities in both spin states compare well with experimental frequencies in the appropriate spectral region. A weak E-symmetry ν(CN) mode lying slightly below the strong absorption in the $HS^{L,tet}$ phase is assigned as an intrinsic feature of the lattice, rather than arising due to minority Fe(LS)-NC-Cr configurations, as has been suggested previously.[7]

(vii) Detailed discussion of the electronic structures of the HS and LS states and the magnetic coupling in the former are presented in the Supplementary Material.[61] The main findings are: first, that the Cr-Cr coupling in the LS state is likely mediated by the mixing of some fraction of the $Fe \rightarrow Cr$ charge transfer excited state into the ground state. Second, that the fundamental absorptions of the LS and $HS^{L,tet}$ states lie in the near UV and low wavelength visible spectral regions, respectively. Both states retain wideband-gap insulating character, in contrast with the finding of Wojdeł *et al.*[27] that the HS phase was metallic. The latter is shown to be a consequence of imposing cubic symmetry in the HS lattice, corresponding to a higher-energy orbital occupancy. Third, that the magnetic coupling in the $HS^{L,tet}$ state is strongly anisotropic, being ferromagnetic within the xy plane and antiferromagnetic along the z axis. However, the averaging of the orientations of the tetragonal distortions within the associated dynamic JT state leads to net ferromagnetic coupling, the axially averaged coupling constant interpolated at $F_0=35\%$ being in good agreement with experiment.[6]

The prospects for related studies combining lattice-dynamics calculations and hybrid functionals are encouraging. Alongside a full treatment of phonon dispersion in the present material, applications to more conventional SCO compounds, such as the solid phases of $Fe(phen)_2(NCS)_2$ and $Fe(pyr)_2[M(CN)_4]$ (M=Ni, Pd, and Pt), are readily envisaged. A more complete model of the SCO cooperativity is also required, as might be provided by the combination of supercell calculations incorporating a greater range of HS site concentrations with determinations of the corresponding vibrational frequencies.

ACKNOWLEDGMENTS

The authors thank S. Margadonna (University of Edinburgh) for useful discussions. D.S.M. and C.C.W. acknowledge the support of the U.K. STFC under Grant No. FDPG/033. D.S.M. and C.P.G. acknowledge the support of the USA NSF under Grant No. CHE0714183. The Research Computing Facility of the EaStCHEM collaboration was used for some of the calculations presented.

*Corresponding author; c.c.wilson@chem.gla.ac.uk

[1] P. Gütlich, Struct. Bonding (Berlin) **44**, 83 (1981).
[2] P. Gütlich, A. Hauser, and H. Spiering, Angew. Chem., Int. Ed. Engl. **33**, 2024 (1994).
[3] E. König, Struct. Bonding (Berlin) **76**, 51 (1991).
[4] O. Kahn and C. J. Martinez, Science **279**, 44 (1998).
[5] A. Bousseksou, K. Boukheddaden, M. Goiran, C. Conséjo, M.-L. Boillot, and J.-P. Tuchagues, Phys. Rev. B **65**, 172412 (2002).
[6] W. Kosaka, K. Nomura, K. Hashimoto, and S. Ohkoshi, J. Am. Chem. Soc. **127**, 8590 (2005).
[7] D. Papanikolaou, W. Kosaka, S. Margadonna, H. Kagi, S. Ohkoshi, and K. Prassides, J. Phys. Chem. C **111**, 8086 (2007).
[8] P. Gütlich and H. A. Goodwin, Top. Curr. Chem. **233**, 1 (2004).
[9] V. Ksenofontov, A. B. Gaspar, and P. Gütlich, Top. Curr. Chem. **235**, 23 (2004).
[10] O. Sato, J. Tao, and Y. Z. Zhang, Angew. Chem., Int. Ed. **46**, 2152 (2007).
[11] M. Sorai, Top. Curr. Chem. **235**, 153 (2004).
[12] B. Papánková, M. Vrbová, R. Boča, P. Šimon, K. Falk, G. Miehe, and H. Fuess, J. Therm Anal. Calorim. **67**, 721 (2002).
[13] A. Bousseksou, J. J. McGarvey, F. Varret, J.-A. Real, J.-P. Tuchagues, A. C. Dennis, and M. L. Boillot, Chem. Phys. Lett. **318**, 409 (2000).
[14] G. Molnár, V. Niel, A. B. Gaspar, J.-A. Real, A. Zwick, A. Bousseksou, and J. J. McGarvey, J. Phys. Chem. B **106**, 9701 (2002).
[15] G. Molnár, T. Kitazawa, L. Dubrovinsky, J. J. McGarvey, and A. Bousseksou, J. Phys.: Condens. Matter **16**, S1129 (2004).
[16] H. Paulsen, H. Winkler, A. X. Trautwein, H. Grünsteudel, V. Rusanov, and H. Toftlund, Phys. Rev. B **59**, 975 (1999).
[17] H. Paulsen, R. Benda, C. Herta, V. Schünemann, A. I. Chumakov, L. Duelund, H. Winkler, H. Toftlund, and A. X. Trautwein, Phys. Rev. Lett. **86**, 1351 (2001).
[18] M. Reiher, Inorg. Chem. **41**, 6928 (2002).
[19] A. Fouqueau, M. E. Casida, L. M. L. Daku, A. Hauser, and F. Neese, J. Chem. Phys. **122**, 044110 (2005).
[20] A. Fouqueau, S. Mer, M. E. Casida, L. M. L. Daku, A. Hauser, and F. Neese, J. Chem. Phys. **120**, 9473 (2004).
[21] L. M. L. Daku, A. Vargas, A. Hauser, A. Fouqueau, and M. E. Casida, ChemPhysChem **6**, 1393 (2005).
[22] J. N. Harvey, Struct. Bonding (Berlin) **112**, 151 (2004).
[23] H. Paulsen and A. X. Trautwein, Top. Curr. Chem. **235**, 197 (2004).
[24] D. Papanikolaou, S. Margadonna, W. Kosaka, S. Ohkoshi, M. Brunelli, and K. Prassides, J. Am. Chem. Soc. **128**, 8358 (2006).
[25] B. Le Guennic, S. Borshch, and V. Robert, Inorg. Chem. **46**, 11106 (2007).
[26] G. Baranović, Chem. Phys. Lett. **369**, 668 (2003).
[27] J. C. Wojdeł, I. P. R. Moreira, and F. Illas, J. Chem. Phys. **130**, 014702 (2009).
[28] G. Brehm, M. Reiher, and S. Schneider, J. Phys. Chem. A **106**, 12024 (2002).
[29] M. Sorai and S. Seki, J. Phys. Chem. Solids **35**, 555 (1974).
[30] R. G. Burns, *Mineralogical Applications of Crystal Field Theory*, 2nd ed. (Cambridge University Press, Cambridge, UK, 1993).
[31] N. Willenbacher and H. Spiering, J. Phys. C **21**, 1423 (1988).
[32] J. Wajnflasz, Phys. Status Solidi **40**, 537 (1970).
[33] C. P. Slichter and H. G. Drickamer, J. Chem. Phys. **56**, 2142 (1972).
[34] R. Dovesi, V. R. Saunders, C. Roetti, R. Orlando, C. M. Zicovich-Wilson, F. Pascale, B. Civalleri, K. Doll, N. M. Harrison, I. J. Bush, P. D'Arco, and M. Llunell, *CRYSTAL06* (University of Torino, Torino, Italy, 2006).
[35] D. S. Middlemiss and C. C. Wilson, Phys. Rev. B **77**, 155129 (2008).
[36] D. S. Middlemiss, L. M. Lawton, and C. C. Wilson, J. Phys.: Condens. Matter **20**, 335231 (2008).
[37] Basis set repository at http://www.crystal.unito.it
[38] A. D. Becke, Phys. Rev. A **38**, 3098 (1988).
[39] S. H. Vosko, L. Wilk, and M. Nusair, Can. J. Phys. **58**, 1200 (1980).
[40] C. Lee, W. Yang, and R. G. Parr, Phys. Rev. B **37**, 785 (1988).
[41] J. Muscat, A. Wander, and N. M. Harrison, Chem. Phys. Lett. **342**, 397 (2001).
[42] F. Corà, M. Alfredsson, G. Mallia, D. S. Middlemiss, W. C. Mackrodt, R. Dovesi, and R. Orlando, Struct. Bonding (Berlin) **113**, 171 (2004).
[43] X. Feng and N. M. Harrison, Phys. Rev. B **70**, 092402 (2004).
[44] I. P. R. Moreira, F. Illas, and R. L. Martin, Phys. Rev. B **65**, 155102 (2002).
[45] C. Franchini, V. Bayer, R. Podloucky, J. Paier, and G. Kresse, Phys. Rev. B **72**, 045132 (2005).
[46] C. Franchini, R. Podloucky, J. Paier, M. Marsman, and G. Kresse, Phys. Rev. B **75**, 195128 (2007).
[47] B. G. Janesko, T. M. Henderson, and G. E. Scuseria, Phys. Chem. Chem. Phys. **11**, 443 (2009).
[48] D. Kasinathan, J. Kuneš, K. Koepernik, C. V. Diaconu, R. L. Martin, I. D. Prodan, G. E. Scuseria, N. Spaldin, L. Petit, T. C. Schulthess, and W. E. Pickett, Phys. Rev. B **74**, 195110 (2006).
[49] A. Stroppa and G. Kresse, Phys. Rev. B **79**, 201201(R) (2009).
[50] A. Janotti, J. B. Varley, P. Rinke, N. Umezawa, G. Kresse, and C. G. Van de Walle, Phys. Rev. B **81**, 085212 (2010).
[51] J. Heyd, J. E. Peralta, G. E. Scuseria, and R. L. Martin, J. Chem. Phys. **123**, 174101 (2005).
[52] M. Marsman, J. Paier, A. Stroppa, and G. Kresse, J. Phys.: Condens. Matter **20**, 064201 (2008).
[53] F. Pascale, C. M. Zicovich-Wilson, F. Lopez, B. Civalleri,

R. Orlando, and R. Dovesi, J. Comput. Chem. **25**, 888 (2004).
[54] C. M. Zicovich-Wilson, F. Pascale, C. Roetti, V. R. Saunders, R. Orlando, and R. Dovesi, J. Comput. Chem. **25**, 1873 (2004).
[55] M. Born and K. Huang, *Dynamical Theory of Crystal Lattices* (Oxford University Press, New York, 1988).
[56] C. M. Zicovich-Wilson, R. Dovesi, and V. R. Saunders, J. Chem. Phys. **115**, 9708 (2001).
[57] W. C. Mackrodt, D. S. Middlemiss, and T. G. Owens, Phys. Rev. B **69**, 115119 (2004).
[58] D. S. Middlemiss and W. C. Mackrodt, Mol. Phys. **103**, 2513 (2005).
[59] J. Kanamori, J. Phys. Chem. Solids **10**, 87 (1959).
[60] J. S. Griffith, *The Theory of Transition Metal Ions* (Cambridge University Press, Cambridge, UK, 1964).
[61] See supplementary material at http://link.aps.org/supplemental/10.1103/PhysRevB.81.184410 for electronic structure in HS and LS states, magnetic coupling in HS state, vibrational eigenvectors for selected Hamiltonians.